Supporting Information

Benign Mid-Gap Halide Vacancy States in 2D-Bismuth-Based Halide Perovskite Microcrystals for Enhanced Broadband Photodetectors

Kuntal Singh[a#], *Mozakkar Hossain*[ab#], *Pabitra Kumar Nayak*[c], *Sougata Karmakar*[a], *Akash Tripathi*[d], *Prakash Sarkar*[a], *Pratyasha Rudra*[e], *A. V. Muhammed Ali*[a], *G. Krishnamurthy Grandhi*[f], *Paola Vivo*[f], *Swastik Mondal*[eg], *K. V. Adarsh*[d], *Dibyajyoti Ghosh*[ch], *K. D. M. Rao*[a*]

[a] *School of Applied & Interdisciplinary Sciences, Indian Association for the Cultivation of Science, Jadavpur, Kolkata 700032, India, E-mail: saiskdmrao@iacs.res.in (K. D. M. R.).*

[b]*Present Address: Department of Mechanical and Aerospace Engineering, University of California, Los Angeles, California 90095, USA*

[c]*Department of Chemistry, Indian Institute of Technology, Delhi, Hauz Khas, New Delhi 110016, India*

[d] *Department of Physics, Indian Institute of Science Education and Research, Bhopal, Madhya Pradesh 462066, India*

[e] *CSIR-Central Glass and Ceramic Research Institute, Kolkata 700032, India*

[f] *Hybrid Solar Cells, Faculty of Engineering and Natural Sciences, P.O. Box 541, FI-33014 Tampere University, Finland*

[g] *Academy of Scientific and Innovative Research (AcSIR), Ghaziabad 201002, India*

[h] *Department of Materials Science and Engineering, Indian Institute of Technology, Delhi, Hauz Khas, New Delhi 110016, India*

Table of content

Experimental section

Synthesis of $Cs_3Bi_2Br_3I_{5.2}$ MCs: The synthesis of facet-oriented 2D-$Cs_3Bi_2Br_3I_{5.2}$ microcrystals (MCs) is performed through a modified hot-spin casting method, as illustrated in **Figure S1**. The precursor solution (0.5 $M.L^{-1}$) in 2 ml of DMSO is prepared by mixing CsI (259.8 mg), $BiBr_3$ (148.7 mg), BiI_3 (194.4 mg), and AgI (29.3 mg) powders, followed by stirring (900 rpm) in a closed vial at 70 °C for 16 hours. The fully dissolved precursor solutions are cooled to room temperature and used for the synthesis of 2D-$Cs_3Bi_2Br_3I_{5.2}$ MCs. The glass substrates of 2.5 × 2.5 cm^2 area are sequentially ultrasonicated for 10 minutes in soap water, milli-Q water, acetone, and IPA, respectively. Subsequently, the UV-ozone-treated glass substrate is pre-heated at 150°C for 8 minutes, followed by spin coating (two-step) with the precursor solution onto cleaned glass substrates (see **Figures S1a** and **S1b**). The precursor solutions are spin-coated (Apex Instruments: SpinNXGP1) on the pre-heated glass substrates. The synthesis of 2D-$Cs_3Bi_2Br_3I_{5.2}$ MCs involves a two-step spin coating process. The first step of spin coating involves spinning at 200 RPM only for 20 seconds, and the second spin coating is performed at 1000 RPM for 60 seconds. Heat transfer from the pre-heated substrate to the precursor solution during spin coating generated heterogeneous nucleation centers at the substrate-solution interface, facilitating subsequent growth. After spin coating, the substrates underwent vacuum drying for 24 hours (see **Figure S1c**), promoting the growth of nucleation centers submerged in a super-saturated precursor solution to form the facet-oriented 2D-$Cs_3Bi_2Br_3I_{5.2}$ MCs. However, the post-heating process to dry the precursor solution led to the formation of non-perovskite and impurity phases due to the mismatch in halide size and electronegativity. Vacuum drying is essential to forming perovskite MCs and mitigating impurity phase formation. Notably, vacuum-assisted slow solvent evaporation extended the time for nuclei center growth, resulting in 2D-$Cs_3Bi_2Br_3I_6$ MCs featuring iodine vacancies, with dimensions ranging between 30 and 200 μm (see **Figure S1d**). The modified hot-spin casting method provides precise control over crystal size (20–300 μm) and facet orientation, enabling the direct synthesis of 2D-$Cs_3Bi_2Br_3I_{5.2}$ without impurity phases.

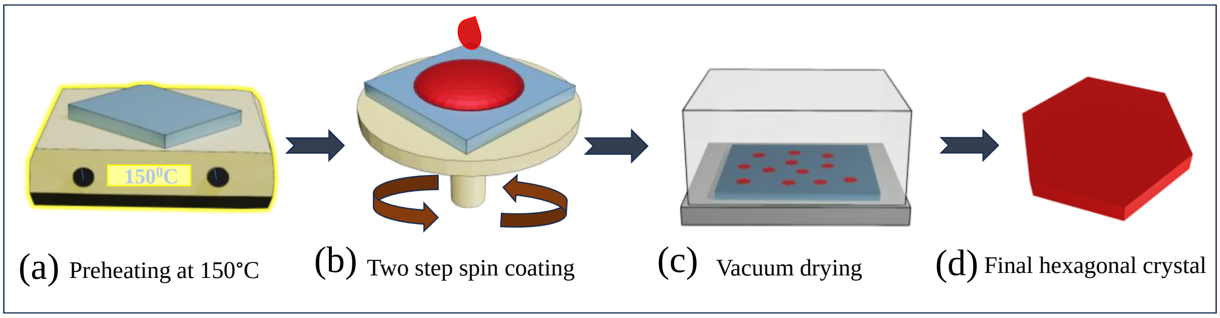

Figure S1: Schematic diagram of the steps involved in the synthesis of 2D-$Cs_3Bi_2Br_3I_{5.2}$ MCs. (a) The glass substrate is preheated at 150°C. (b) Two-step spin coating on the preheated substrate. (c) Slow vacuum drying in an evacuated chamber. (d) Schematic representation of hexagonal 2D-$Cs_3Bi_2Br_3I_{5.2}$ MCs.

Characterization of iodide deficient $Cs_3Bi_2Br_3I_{5.2}$ MCs: Single crystal X-ray diffraction (XRD) analysis of $Cs_3Bi_2Br_3I_{5.2}$ MCs is performed at room temperature, irradiating with Mo Kα (λ = 0.7107 Å) from a Bruker D8 VENTURE 431 with a 1μS 3.0 microfocus X-ray source. Diffracted data is collected through a CMOS detector equipped with the Bruker D8 VENTURE using the software package APEX III. Additionally, Powder X-ray diffraction patterns of $Cs_3Bi_2Br_3I_{5.2}$ MCs are obtained using Bruker AXS D8 Advanced equipment (40 kV, 40 mA, wavelength ~ 0.15406 nm) with Cu Kα radiation. Scanning electron microscopy (SEM) and EDX elemental mapping measurements are executed with FESEM (JEOL JSM-7500F). SAED patterns are measured with the transmission electron microscope (JEOL, JEM 2100 F). Defused reflectance spectra are recorded using Agilent carry 5000 UV-VIS- NIR and converted to UV-vis absorption spectra using $F(\alpha) = \frac{k}{s} = \frac{(1-R_\infty)^2}{2R_\infty}$.[1] Temperature-dependent photoluminescence (PL) spectra and Raman spectra are collected by using the Raman Triple spectrometer Jobin-Yvon T64000 by exciting the sample with Nd:YAG green laser (532.5 nm, ~ 10 μW power). The confocal microscope images are captured using Zeiss LSM 800 with a GaAsP PMT detector with an excitation wavelength of 561 nm. X-ray photoelectron spectroscopy (XPS) and Ultra-photoelectron Spectroscopy (UPS) measurements are carried out using a PHI 500 Versa Probe-III instrument with a photon energy of 21.2 eV.

Fabrication of $Cs_3Bi_2Br_3I_{5.2}$ MC-based photodetector: The fabrication of the $Cs_3Bi_2Br_3I_{5.2}$ MC-based photodetector involves the use of an asymmetric gap electrode (ITO/Au), where Au electrodes are deposited on etched ITO glass through thermal evaporation using a Hind High Vacuum Company Private Limited system (Model: 12A4D). Micro imprint lithography is employed to transfer $Cs_3Bi_2Br_3I_{5.2}$ MCs onto the asymmetric gap electrode, utilizing a thick PDMS mold and a few drops of isopropanol (IPA) to ensure efficient transfer onto the substrate. The active area of the photodetector is approximately 890×10^{-12} m^2. Current-voltage characteristics and photocurrent measurements are performed using a Keithley 2634B system connected to a Lakeshore PS-100 probe station. Wavelength-dependent photocurrent measurements are conducted using an F4 spectral illumination system, while transient photo-response is measured by modulating light intensity at different frequencies with a Scientific Instruments SM5070 function generator connected to white LEDs. I-V measurements for modified Hecht equation are carried out in a symmetric in-plane geometry ($Au/MoO_3/Cs_3Bi_2Br_3I_{5.2}/MoO_3/Au$), with 20 nm MoO3 layer and 50 nm Au electrodes separated by 60 μm. A 95 × 180 μm^2 device area was used for transient photocurrent measurements.

Computational Methodology: All DFT-based simulations employed the widely used Vienna Ab Initio Simulation Package (VASP), incorporating a Projected Augmented Wave (PAW) methodology for ion-electron interactions.[2–4] The selected cut-off energy for the plane wave basis set was established at 520 eV to facilitate structural relaxation, with the geometry adjusted until the interionic force diminished below 0.01 eV/Å.[5] The semi-local Perdew-Burke-Ernzerhof (PBE) function within the framework of Generalized Gradient Approximation (GGA) is adopted for the exchange-correlation interaction in the simulations.[6] A Γ-centered 4 × 4 × 2 and 9 × 9 × 5 Monkhorst-Pack k-point mesh was utilized for cell relaxation and electronic properties calculation, respectively.[7] Additionally, static structural bond-parameter assessments are conducted using VESTA software.[8] Electronic property analyses for $Cs_3Bi_2Br_3I_6$ and $Cs_3Bi_2Br_3I_5$ are performed through SUMO.[9] For ab initio molecular dynamics (AI-MD) simulations, we constructed a 2 × 2 × 2 supercell comprising 8 formula units and a total of 112 atoms and 104 atoms for pristine $Cs_3Bi_2Br_3I_6$ and $Cs_3Bi_2Br_3I_5$. A single Gamma-point mesh was utilized, along with a time step of 1 fs and a plane-wave energy cutoff of 400 eV. The AIMD simulations began with the DFT-optimized structure, which was incrementally heated to 300 K through repeated velocity rescaling over 3 ps. To ensure thermal equilibrium, an additional 4 ps of trajectory data was generated using the canonical ensemble. Finally, we performed 3.5 ps of simulations under the microcanonical ensemble, and the resulting trajectory was employed for structural dynamics and thermal stability analysis.

Table S1: Crystal structure refinement parameters of 2D $Cs_3Bi_2Br_3I_{5.2}$ MC using single crystal X-ray diffraction (SCXRD) measurements.

Empirical formula	**$Cs_3Bi_2Br_3I_{5.2}$**
Formula weight	1718.84
Temperature/K	180.15
Crystal system	Trigonal
Space group	P-3m1
a/Å	8.2207(12)
b/Å	8.2207(12)
c/Å	10.104(2)
α/°	90
β/°	90
γ/°	120
Volume/$Å^3$	591.3(2)
Octahedral Volume/$Å^3$	33.5601
Z	1
Density (calculated) g/cm^3	4.827
Absorption coefficient (μ)/mm^{-1}	31.266
Radiation	MoK_α (λ = 0.71073)
Goodness-of-fit	1.164
Final R indexes [I>=2σ (I)]	$R_1 = 0.0184$, $wR_2 = 0.0425$
Final R indexes [all data]	$R_1 = 0.0196$, $wR_2 = 0.0431$
Largest diff. peak/hole / e $Å^{-3}$	0.73/-0.65

Table S2: Fractional atomic coordinates ($\times10^4$) and equivalent isotropic displacement parameters (Å$^2\times10^3$) of 2D $Cs_3Bi_2Br_3I_{5.2}$ MCc, Ueq is defined as 1/3 of the trace of the orthogonalized U_{ij} tensor.

Atom	**Wyckoff sites**	***x***	***y***	***z***	**U(eq)***
Bi1	2d	3333.33	6666.67	3170.8(3)	34.32(15)
Cs2	2d	6666.67	13333.33	1788.5(9)	72.1(3)
Cs1	1b	0	10000	5000	77.7(4)
I1	6i	1647.2(4)	8352.8(4)	1634.3(6)	66.8(3)
Br1	3f	5000	5000	5000	84.9(4)

Table S3: Anisotropic displacement parameters (Å$^2\times10^3$) for 2D-$Cs_3Bi_2Br_3I_{5.2}$ MC Anisotropic displacement factor exponent takes the form: $-2\pi^2[h^2a^{*2}U_{11}+2hka^*b^*U_{12}+\ldots]$.

Atom	**U11**	**U22**	**U33**	**U23**	**U13**	**U12**
Bi1	35.91(17)	35.91(17)	31.1(2)	0	0	17.95(9)
Cs2	71.4(4)	71.4(4)	73.7(6)	0	0	35.7(2)
Cs1	81.2(6)	81.2(6)	70.8(9)	0	0	40.6(3)
I1	73.6(4)	73.6(4)	66.9(8)	10.94(14)	10.94(14)	47.1(4)
Br1	106.3(8)	106.3(8)	74.8(8)	17.2(3)	-17.2(3)	77.7(9)

Table S4: Bond distance parameters (Å) for 2D-$Cs_3Bi_2Br_3I_{5.2}$ microcrystal

$Cs_3Bi_2Br_3I_{5.22}$		
Atom1	**Atom2**	**Length (Å)**
Bi1(1)	I1(1)	2.8590(6)
Bi1(1)	I1(2)	2.8590(6)
Bi1(1)	Br1(1)	3.0079(4)
Bi1(1)	Br1(2)	3.0079(4)
Cs2(1)	I1(1), I1(3), I1(4), I1(6) and I1(7)	4.1134(6)
Cs2(1)	I1(5), I1(8), I1(4), I1(6) and I1(7)	4.2101(11)
Cs2(1)	Br1	4.0201(9)
Cs1	I(1)	4.1311(9)
Cs1	Br1	4.1104(6)

Table S5: Bond angle parameters (Å) for 2D $Cs_3Bi_2Br_3I_{5.2}$ microcrystal

$Cs_3Bi_2Br_3I_{5.22}$	
Atom1-Atom2 -Atom3	**Angle (Degree)**
Bi1-Br1-Bi1	180.0000(0)
I1-Bi1-Br1	174.967(19)

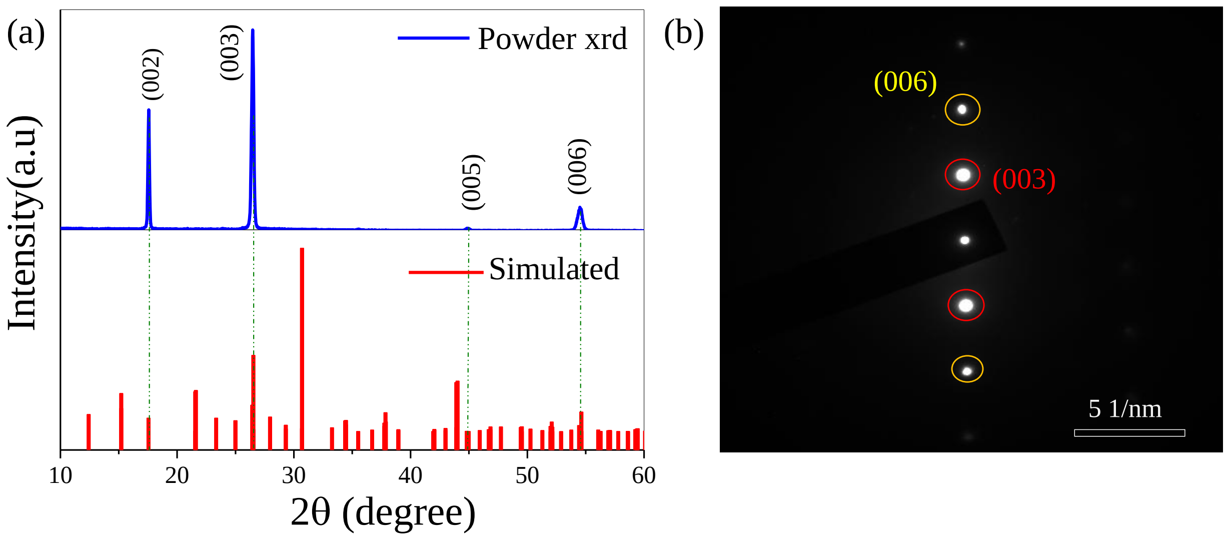

Figure S2. Structural Characterization of $Cs_3Bi_2Br_3I_{5.2}$ MCs. (a) Experimental powder XRD patterns at room temperature of 2D $Cs_3Bi_2Br_3I_{5.2}$ compared with simulated XRD patterns. (b) TEM SAED pattern of 2D $Cs_3Bi_2Br_3I_{5.2}$ MCs providing single crystal nature.

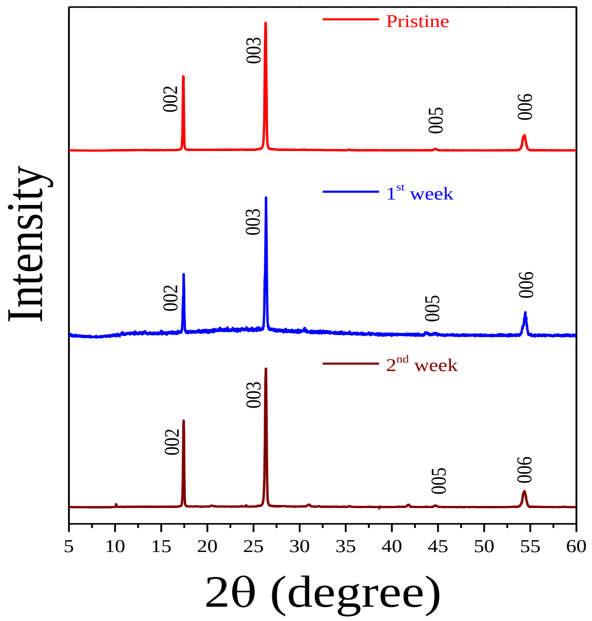

Figure S3. Time-dependent XRD of 2D-$Cs_3Bi_2Br_3I_{5.2}$ MCs after exposure to the ambient environment for two weeks

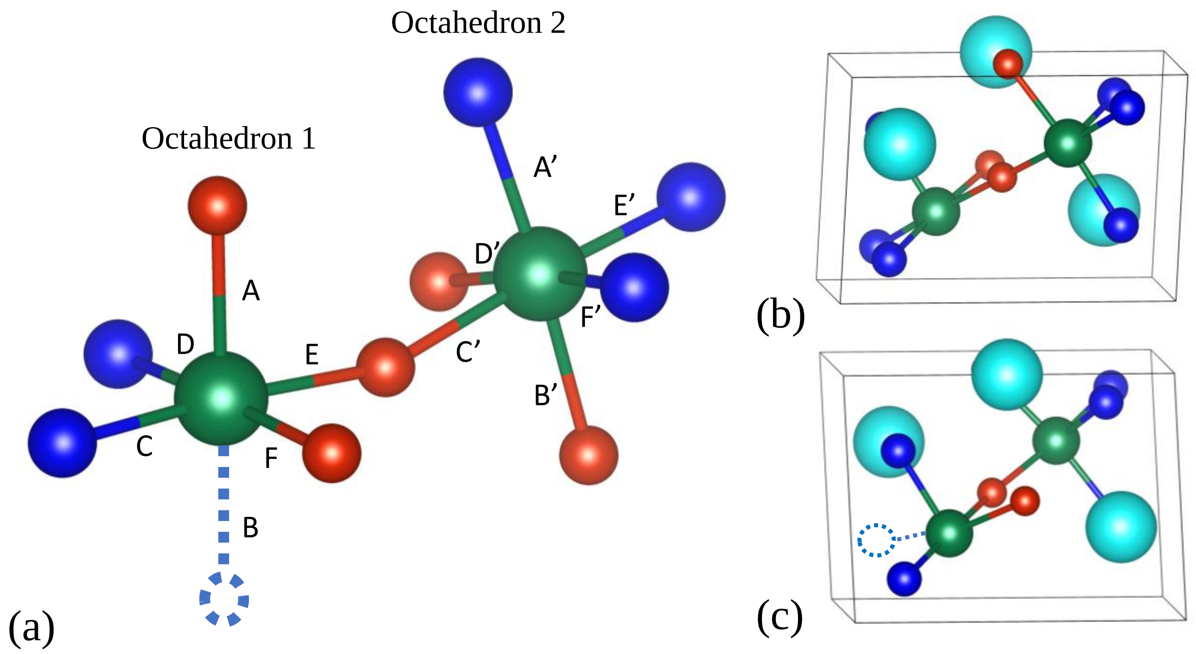

Figure S4. (a) The connected octahedra are shown after creating an I-vacancy (shown as dotted lines). Capital alphabets represent the nomenclature of bonds, and the bond angles are determined by the bonds involved in forming that particular angle. For example, the inter-octahedral angle involves the E and C' bonds, thus named as E-C'. (b) and (c) depict schematics of pristine $Cs_3Bi_2Br_3I_6$ and I-vacancy $Cs_3Bi_2Br_3I_6$, respectively.

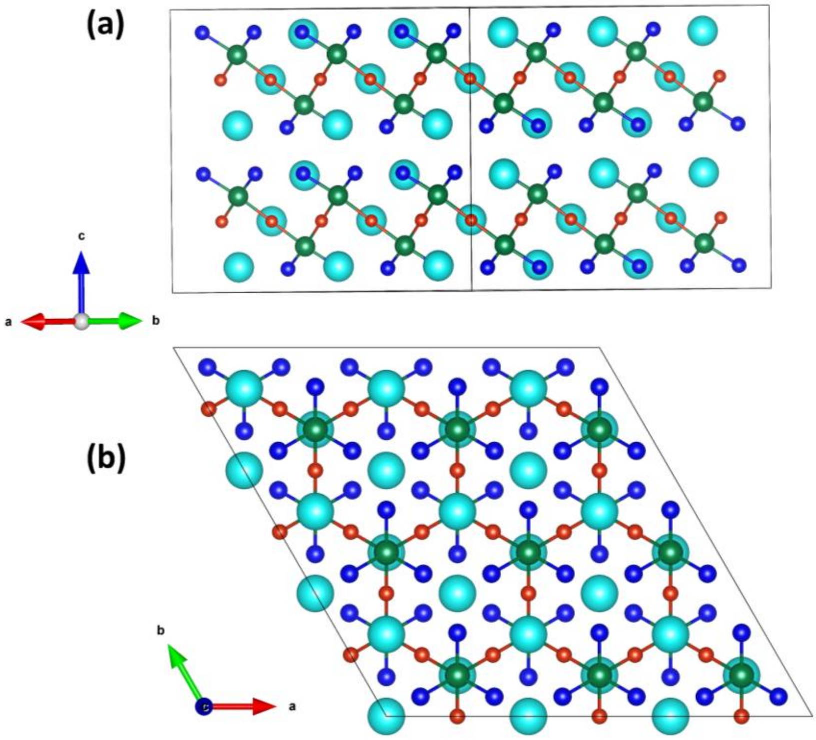

Figure S5. The (a) side view and (b) top view of pristine $Cs_3Bi_2Br_3I_6$. (a) shows that the iodine atoms occupy positions along the edges of the layered structure, and the bromine atoms form bonds with neighboring octahedra. (b) shows the symmetrical arrangement of all iodine and bromine maintaining an equivalent chemical environment, allowing us to select any iodine atom for removal to model the iodine vacancy.

Table S6: Structural parameters include bond lengths of optimized (using DFT-based simulation) geometry of $Cs_3Bi_2Br_3I_6$ and $Cs_3Bi_2Br_3I_5$ MCs at 0K. Follow **Figure S4a** for the nomenclature of the bond and bond angles.

	Octahedron 1			Octahedron 2	
Bond length (Å)	**Pristine**	**I-defect**	**Bond length (Å)**	**Pristine**	**I-defect**
A	2.98	3.11	A’	2.94	3.03
B	2.94	--	B’	2.98	2.98
C	2.94	2.96	C’	2.98	3.03
D	2.94	2.96	D’	2.98	3.03
E	2.98	2.98	E’	2.94	2.96
F	2.98	2.98	F’	2.94	3.96

Table S7: Structural parameters include bond angles of optimized (using DFT-based simulation) geometry of $Cs_3Bi_2Br_3I_6$ and $Cs_3Bi_2Br_3I_5$ 2D-MHP MCs at 0K. Follow **Figure S4a** for the nomenclature of the bond and bond angles.

Inter-Octahedral	**Octahedron 1**			**Octahedron 2**	
Bond Angle (°)	**Pristine**	**I-defect**	**Bond Angle (°)**	**Pristine**	**I-defect**
A-B	175.66	--	A’-B’	175.66	175.99
C-E	175.66	175.65	C’-E’	175.66	173.49
D-F	175.66	175.65	D’-F’	175.66	173.49
Inter-Octahedral	Pristine		I-defect		
E-C’	180		160.61		

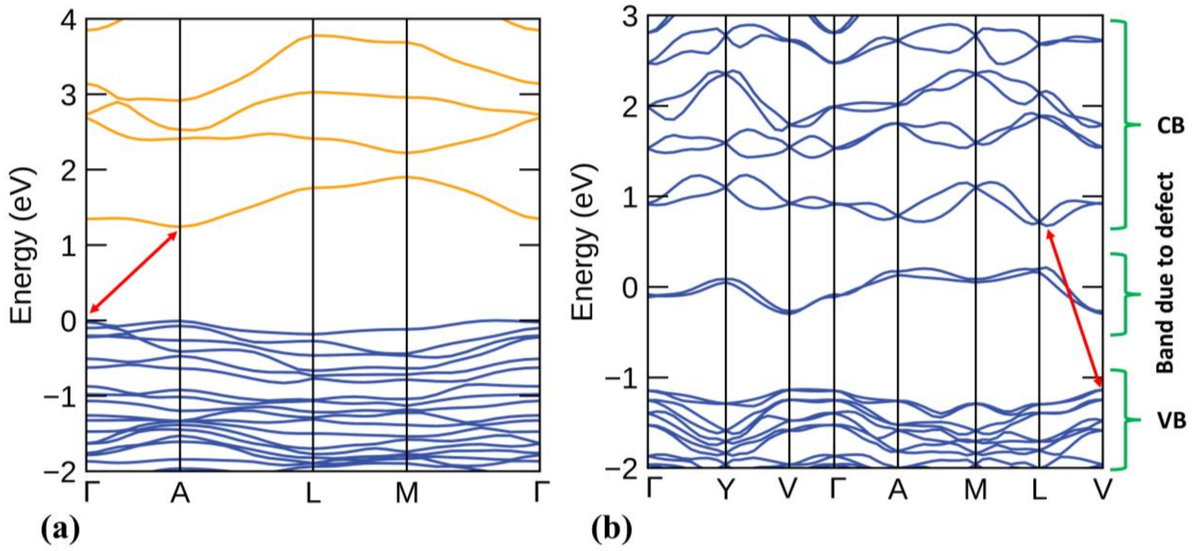

Figure S6. Band structure plot for (a) pristine $Cs_3Bi_2Br_3I_6$ and (b) $Cs_3Bi_2Br_3I_5$ considering PBE functional with spin-orbit coupling effects. The systematic underestimation of the band gap (compared to Figure 2) appears due to the usage of the semi-local PBE exchange-correlation functional in these simulations.

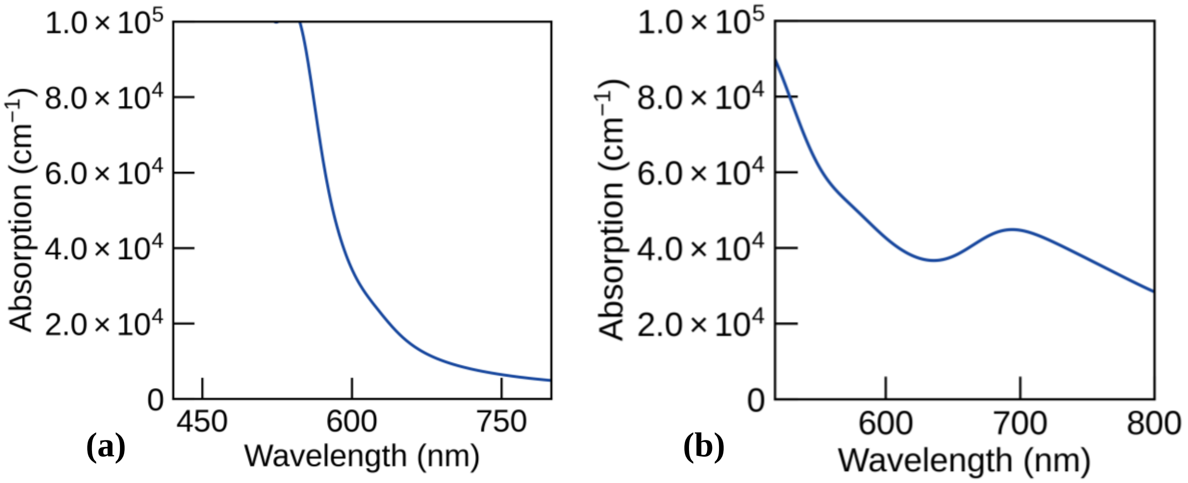

Figure S7: Simulated absorption spectra of pristine $Cs_3Bi_2Br_3I_6$ and $Cs_3Bi_2Br_3I_5$ with an I-vacancy

I6.mp4

Video S1. Thermal fluctuation of pristine $Cs_3Bi_2Br_3I_6$ over a 3.5 ps timeframe.

I5.mp4

Video S1. Thermal fluctuation of pristine $Cs_3Bi_2Br_3I_5$ over a 3.5 ps timeframe.

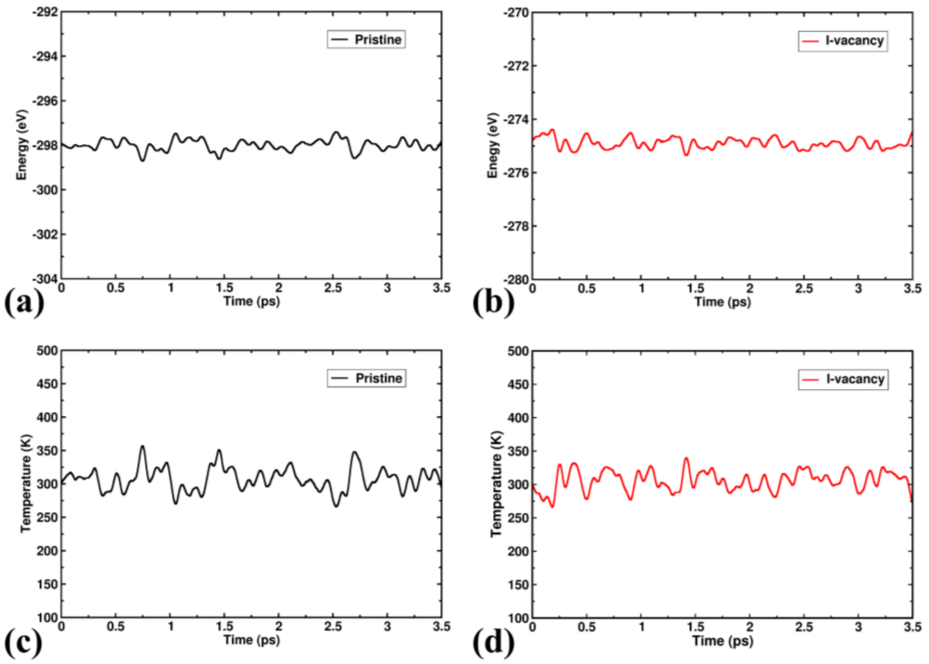

Figure S8. Evolution of potential energy over 3.5 ps trajectories in a microcanonical ensemble of (a) pristine ($Cs_3Bi_2Br_3I_6$) and (b) I-vacancy ($Cs_3Bi_2Br_3I_5$) materials. Similarly, temperature fluctuation over the trajectories for (c) pristine ($Cs_3Bi_2Br_3I_6$) and (d) I-vacancy ($Cs_3Bi_2Br_3I_5$) materials.

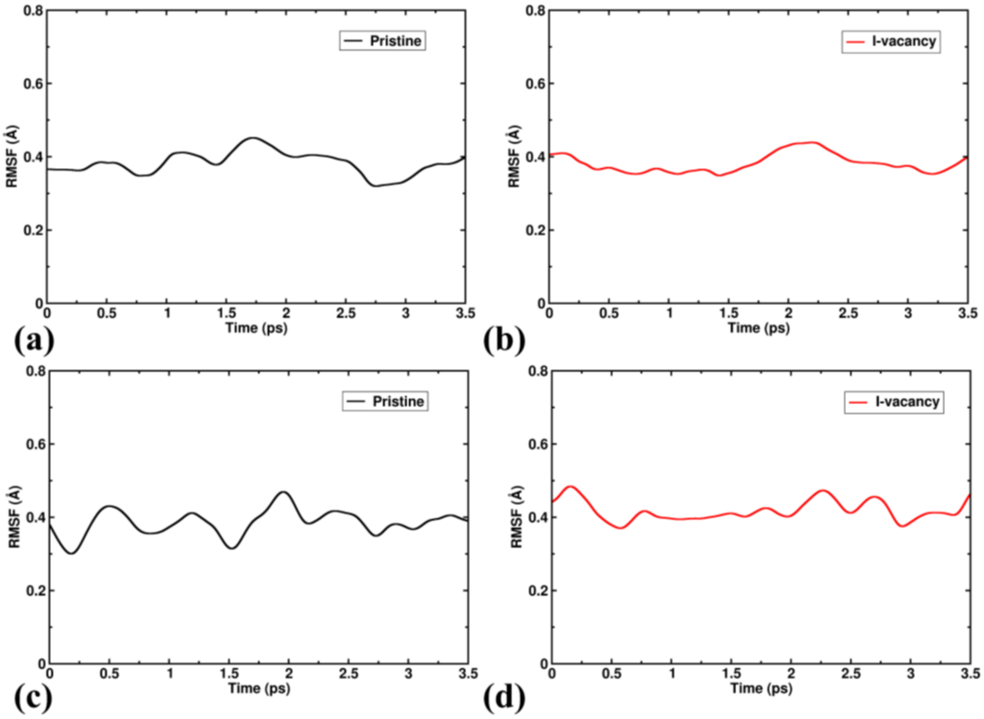

Figure S9. Root Mean Square Fluctuation (RMSF) of overall material over the 3.5 ps time for (a) pristine ($Cs_3Bi_2Br_3I_6$) and (b) I-vacancy ($Cs_3Bi_2Br_3I_5$) materials. RMSF of Cs atoms over the trajectories for (c) pristine ($Cs_3Bi_2Br_3I_6$) and (d) I-vacancy ($Cs_3Bi_2Br_3I_5$) materials.

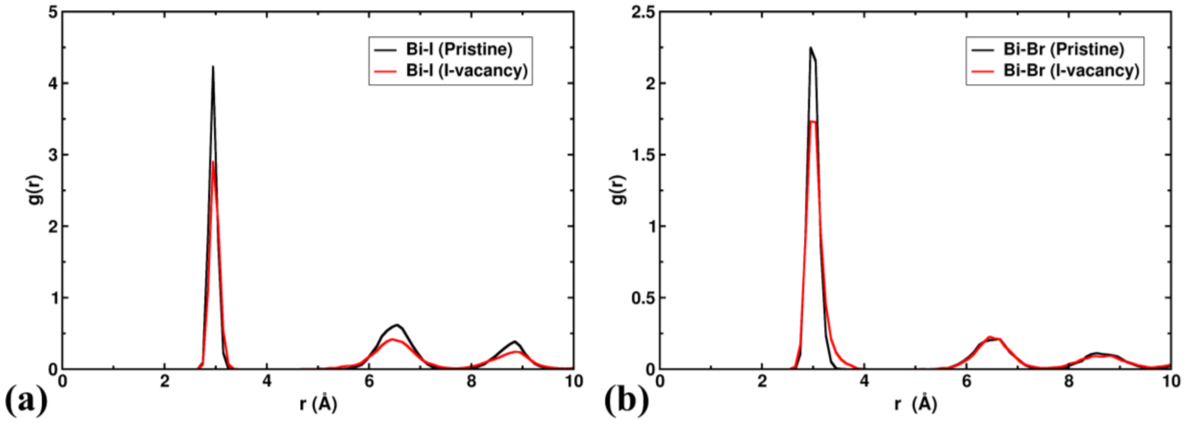

Figure S10. Radial distribution of iodine atoms with respect to Bi atoms for (a) pristine ($Cs_3Bi_2Br_3I_6$) and I-vacancy materials ($Cs_3Bi_2Br_3I_5$). Similarly, the radial distribution of bromine atoms with respect to bismuth atoms for (b) pristine ($Cs_3Bi_2Br_3I_6$) and I-vacancy materials ($Cs_3Bi_2Br_3I_5$).

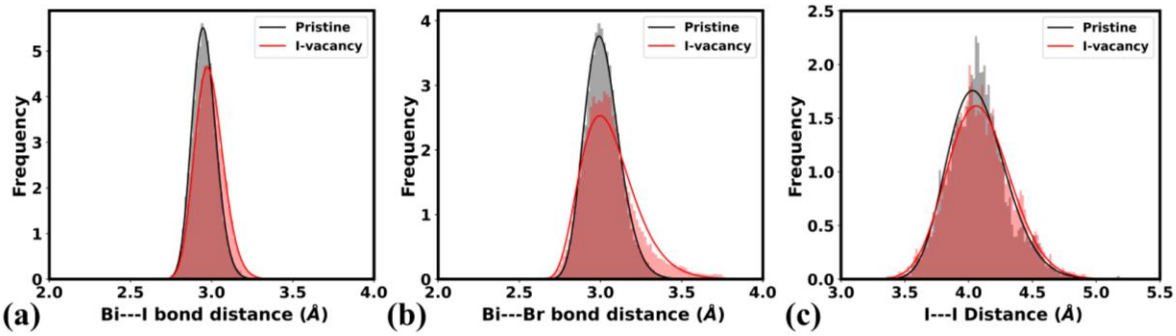

Figure S11. The histogram distribution plots of (a) intra-octahedral Bi-Br bond distances, (b) intra-octahedral Bi-I bond distances, and (c) interlayer I-I distance (terminal I-I distance across the layer along the c-direction).

Section 1: Both materials show thermal stability, with the potential energy remaining stable throughout the simulation, confirming the preservation of the layered structure over time. The temperature fluctuations are centered around 300 K for both pristine $Cs_3Bi_2Br_3I_6$ and $Cs_3Bi_2Br_3I_5$ (**Figure S8**). The root means square fluctuations (RMSFs) of overall materials and Cs atoms show very minimal deviation of atoms from the crystal lattice, illustrating the structural stability (**Figure S9**). The radial distribution of bromine and iodine atoms with respect to bismuth atoms (**Figure S10**) and the histogram plot of Bi-I and Bi-Br bond distance over the MD- trajectories (**Figure S11)** shows that all the iodine and bromine atoms maintain their lattice position with minimal deviation (standard deviations (SD) 0.07-0.17 Å). Similarly, the histogram plot of interlayer I…I distance atoms analysis (SD: 0.23/0.24 Å) further supports the thermal stability of these materials (**Figure S11c**).

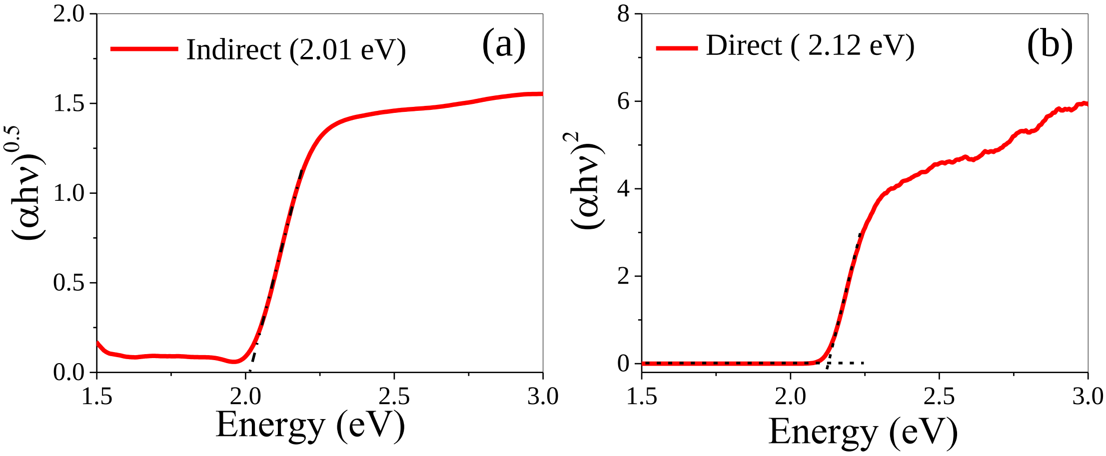

Figure S12. Tauc plot from UV-Vis absorption spectra to estimate the (a) indirect and (b) direct bandgap of 2D-$Cs_3Bi_2Br_3I_{5.2}$ MCs.

Section 2: The bandgap of 2D-$Cs_3Bi_2Br_3I_{5.2}$ is calculated from Tauc plot analysis following the below equation.[1]

$$(\alpha h\nu)^{\frac{1}{n}} = A\left(h\nu - E_g\right) - - - - - - - - - - - - - - (1)$$

Where α, h, ν, A, and Eg represent the absorption coefficient (cm^{-1}), Planck's constant, frequency, constant, and optical bandgap, respectively. Here, n is a dimensionless parameter, set to 2 for an indirect bandgap and ½ for a direct bandgap. From the Tauc plot in **Figure S12**, the indirect and direct bandgaps of 2D-$Cs_3Bi_2Br_3I_{5.2}$ are determined as 2.03 and 2.12, respectively, which aligns closely with the reported 2 eV bandgap of 2D-$Cs_3Bi_2Br_3I_6$.

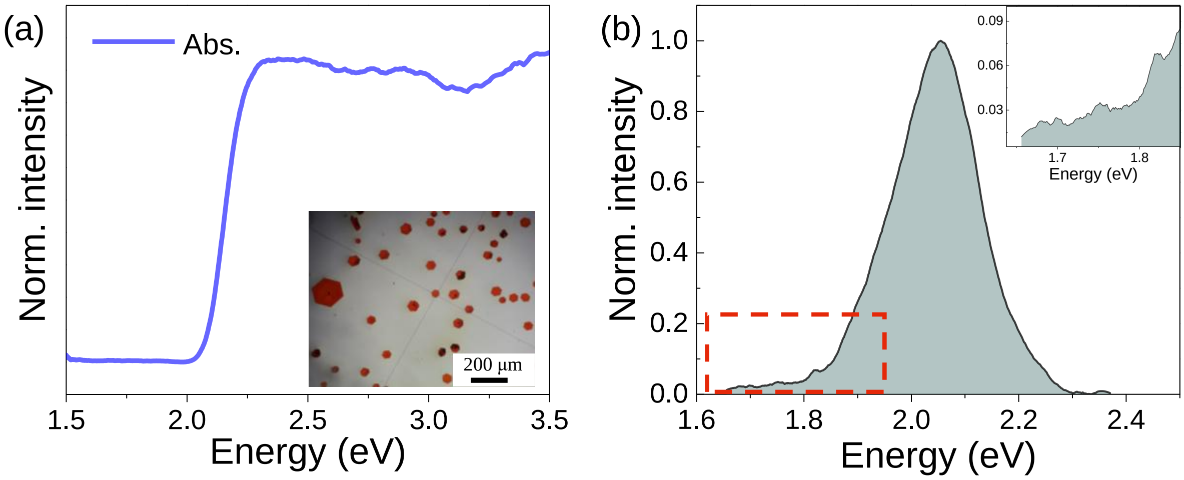

Figure S13. (a) UV-vis absorption spectrum of $Cs_3Bi_2Br_3I_{5.2}$ microcrystals obtained via diffuse reflectance spectroscopy. Inset: Optical microscopy image of $Cs_3Bi_2Br_3I_{5.2}$ MCs on a glass substrate. (b) Photoluminescence (PL) spectrum of $Cs_3Bi_2Br_3I_{5.2}$ MCs collected using a microfocus laser system. Inset: Magnified view of the PL spectrum at lower energy.

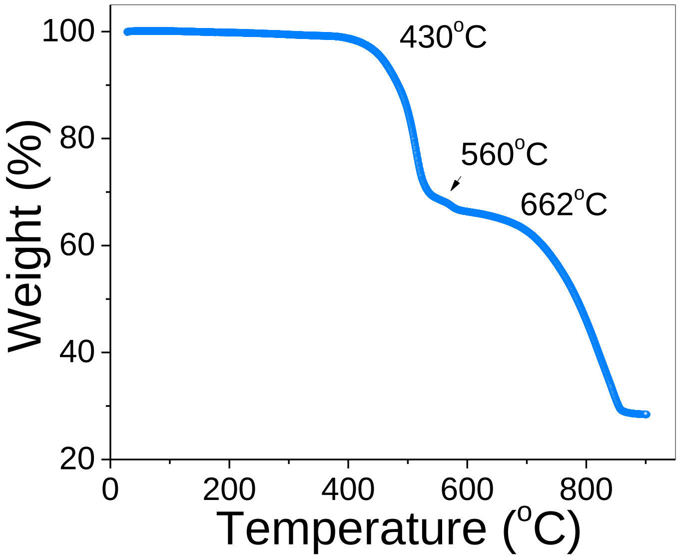

Figure S14. Thermogravimetric analysis of 2D $Cs_3Bi_2Br_3I_{5.2}$ MCs

Thermogravimetric analysis is performed in a nitrogen atmosphere to evaluate the thermal stability of 2D $Cs_3Bi_2Br_3I_{5.2}$ MCs. The study spanned temperatures from 30°C to 900°C, with a heating rate of 10°C per minute, as depicted in **Figure S14**. Initially, weight loss was noted at 430°C, followed by subsequent losses at 560°C, corresponding to the sublimation of BiI_3 and $BiBr_3$, respectively.[10,11] 33% of the weight loss is observed within this temperature range. A notable decline in weight is observed at 662°C, attributed to the loss of CsI material.[11] Thus, the material exhibits commendable thermal stability at elevated temperatures.

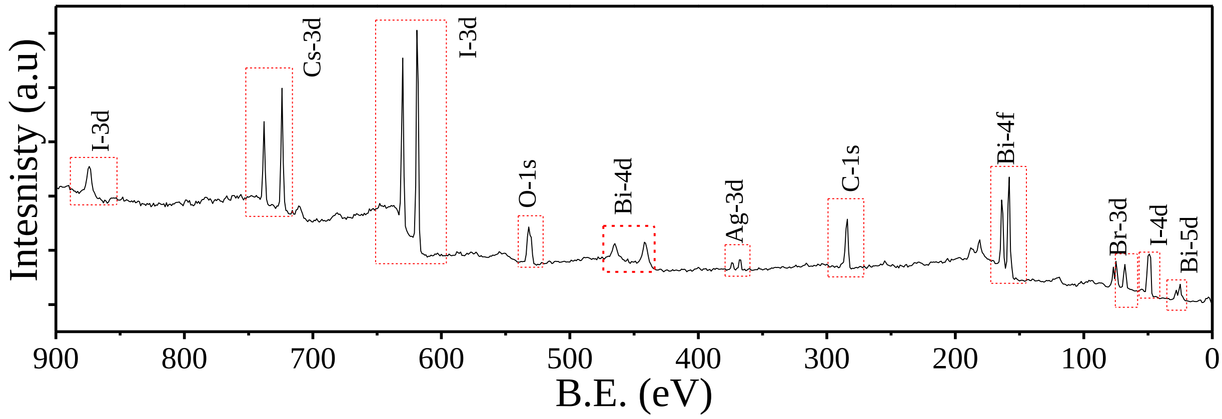

Figure S15. X-ray photoelectron spectroscopy (XPS) survey spectra of 2D-$Cs_3Bi_2Br_3I_{5.2}$ MC.

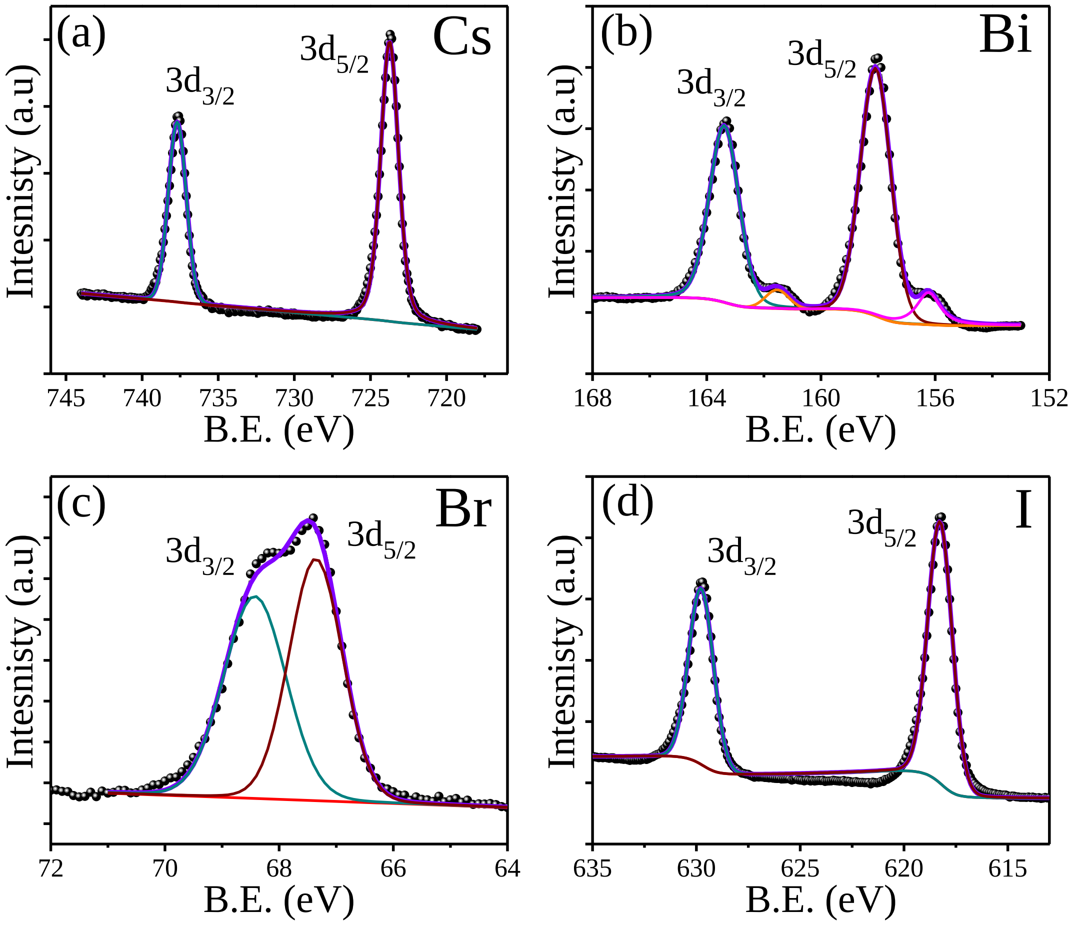

Figure S16. Core level XPS spectra of (a) Cs 3d, (b) Bi 4f, (c) Br 3d, and (d) I 3d in 2D-$Cs_3Bi_2Br_3I_{5.2}$ MC.

Table S8: Estimation of atomic ratios of constituent elements in 2D $Cs_3Bi_2Br_3I_{5.2}$ from core level XPS spectra

Elements	**States**	**Peak position (eV)**	**Area**	**RSF Value**	**Total area**	**No. of scan**	**Area per single scan**	**Stoichiometric ratio**	**Ideal ratio**
Cs^+	$3d_{5/2}$	724.29	71153.9	23.76	5450.3	5	1090.0	2.27	3
	$3d_{3/2}$	738.27	40422.4	16.46					
Bi^{3+}	$4f_{7/2}$	158.25	55340.6	13.9	7683.3	8	960.37	2	2
	$4f_{5/2}$	163.54	40468.7	10.93					
Br-	$3d_{5/2}$	68.42	14344.4	1.68	20563.9	15	1370.9	2.9	3
	$3d_{3/2}$	69.47	12376.4	1.16					
I^-	$3d_{5/2}$	618.33	128448	19.87	12720.5	5	2544.1	5.29	5.2
	$3d_{3/2}$	629.73	86147.6	13.77					

Ag	3d5/2	367.23	29010.4	10.66	5143.93	25	205.75	0.42	-
	3d3/2	373.24	17878.3	7.38					

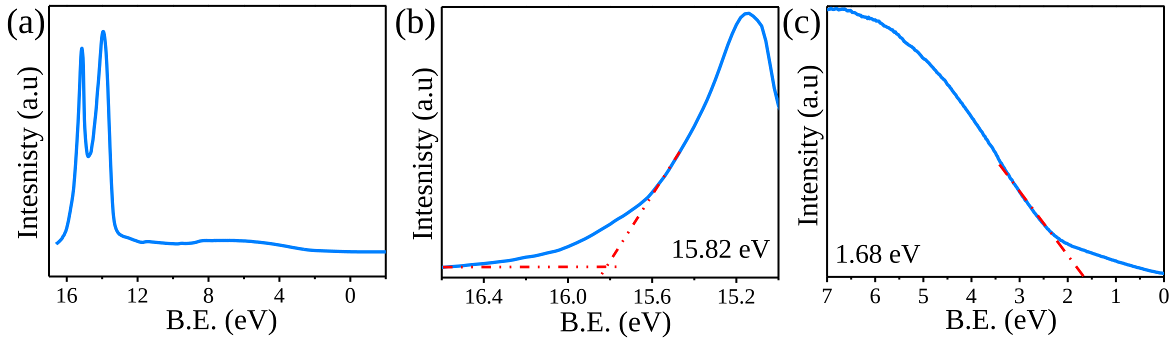

Figure S17. (a) UPS survey spectra of iodide deficient 2D $Cs_3Bi_2Br_3I_{5.2}$ MCs. (b) High energy UPS cut-off region, (c) low energy UPS tail onset region.

Table S9: Electronic Band levels of 2D $Cs_3Bi_2Br_3I_{5.2}$ micro crystals, calculated from UPS spectra

Work Function (E_F)	**E_F -E_{VBM}**	**E_{VBM}**	**Bandgap (E_g)**	**E_{CBM}**	**Semiconducting type**
5.38	1.68	7.06	2.03	5.03	n-type

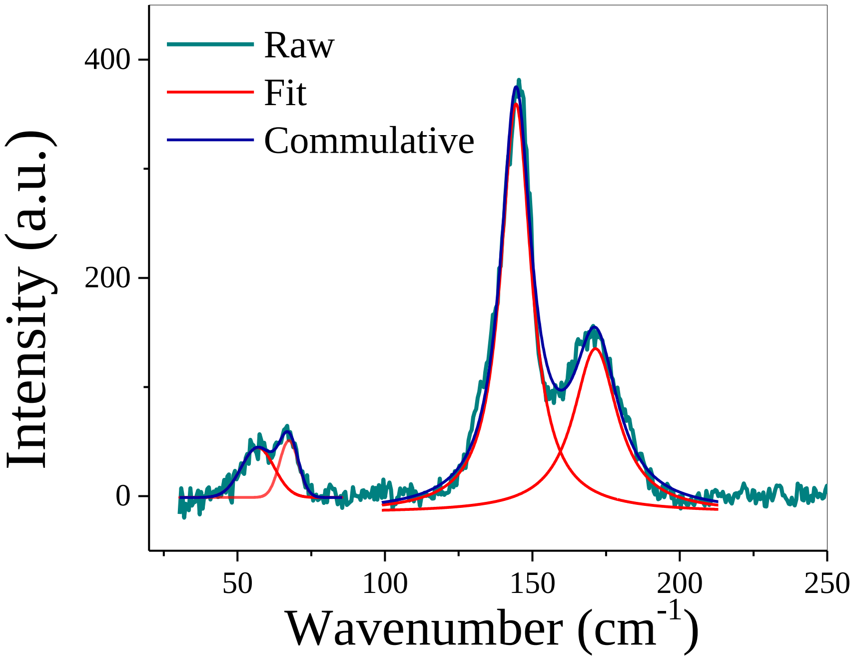

Figure S18. Raman spectra of 2D-$Cs_3Bi_2Br_3I_{5.2}$ MC recorded with a 530 nm excitation wavelength.

Table S10: Details of Raman spectra of $Cs_3Bi_2Br_3I_{5.2}$

Symmetry	Description	Wavenumber (cm^{-1})	Energy (meV)	Ref.
E_{2g}	Bridge Bi–Br symmetric stretch	169.06	21.11	12
A_{1g}	terminal Bi–I symmetric stretch	145.46	18.16	13
E_g	Bi-Br bending mode	66.83	8.34	12
A_{1g}	Bi-I bending mode	57.47	7.17	13

Section 3: Details of the calculation of trap density (η_{trap}) and mobility (μ).

$$\eta_{trap} = \frac{2\varepsilon_0 \varepsilon V_{TFL}}{q l^2} - - - - - - - - (S2)^{14}$$

$$J_d = \frac{9}{8}\varepsilon_0 \varepsilon \mu \frac{V^2}{l^3} - - - - - - - - (S3)^{15}$$

where, η_{trap} = trap density (cm^{-3})

ε_0 = free space permittivity

ε = relative dielectric constant of perovskite (12.47 for $Cs_3Bi_2Br_3I_6$)

q = elementary charge

l = Gap between two electrodes, 55 μm.

J_d= current density

μ = carrier mobility

V = applied voltage

Section 4: Details of photoconductivity and diffusion length (L_D) calculation.

$$I = \frac{I_0 \mu\tau V}{l^2}\frac{1-\exp\left(-\frac{l^2}{\mu\tau V}\right)}{1+\frac{lS}{\mu V}} - - - - - - - - - - - (S4)$$ [16]

$$L_D = \sqrt{\frac{k_B T \mu\tau}{e}} - - - - - - - - - - - - - - (S5)$$ [17]

Where, I = photocurrent

I_0 = saturated photocurrent

$\mu\tau$ = mobility-lifetime product

l = Gap between two electrodes, 55 µm

V = applied voltage

S = surface recombination velocity

k_B = Boltzmann constant

T = sample temperature

e = elementary charge

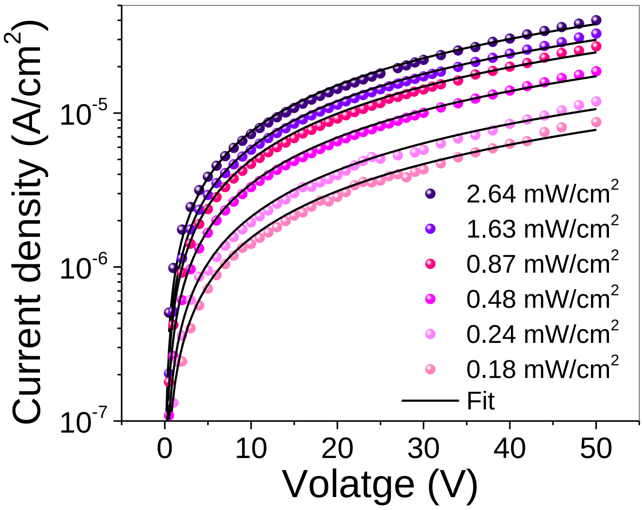

Figure S19. Fitting of photocurrent as a function of voltage using the modified Hecht equation under various light intensities (0.18 to 2.64 mW/cm²).

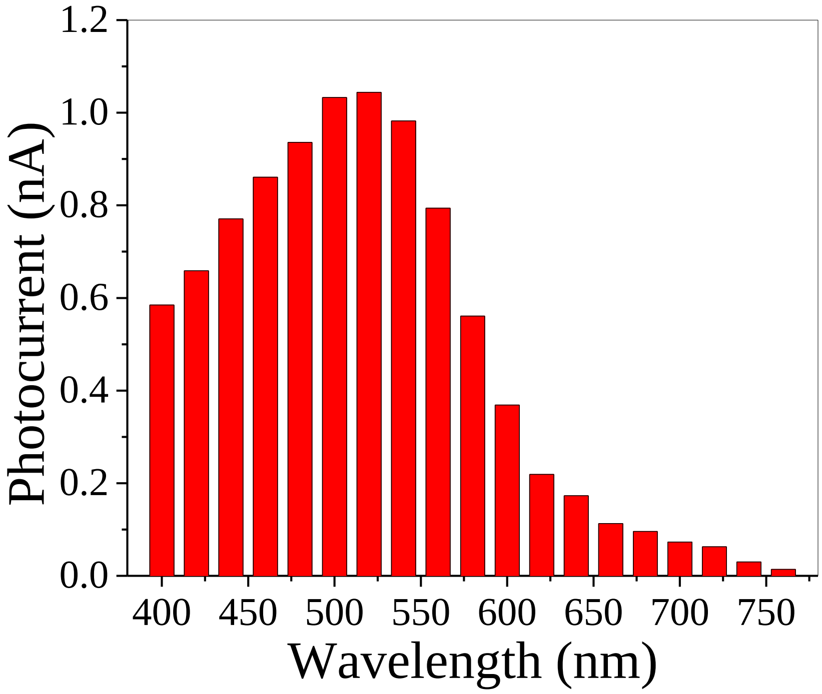

Figure S20: Photocurrent of 2D-$Cs_3Bi_2Br_3I_{5.2}$ MC-based photodetector across the wavelength range from 400 nm to 800nm.

Section 5: Photodetector figure of merit (FOM) estimation

Responsivity (R_λ)[18]

$$R_\lambda = \frac{J_{ph}}{P_{Light}} ------------ (S6)$$

$$J_{ph} = \frac{I_{ph}}{A} -------------(S7)$$

Where, R_λ= responsivity

J_{ph}= photocurrent density

I_{ph}= I_l - I_d = photocurrent

I_l= light current

I_d= dark current

P_{Light}= light intensity

A = active area of the device

Detectivity (D)[18]

$$D = \frac{R_\lambda}{\sqrt{2qJ_d}} -------------(S8)$$

Where, D= Detectivity

R_λ= responsivity

q = charge of the electron

Details of Noise Equivalent Power (NEP).[18]

$$NEP = \frac{S_I}{R_\lambda} - - - - - - - - - - - (\mathrm{S9})$$

$$S_I = \sqrt{\frac{<{I_{noise}}^2>}{1\ Hz}} - - - - - - - - (\mathrm{S10})$$

Where, NEP = Noise equivalent power

S_I = RMS value of dark current density at 1 Hz bandwidth

I_{noise} = dark current

R_λ = wavelength-dependent responsivity

Rise and fall time calculation.[18]

$$I = I_0 - I_0 \times e^{\left(-\frac{x}{t_r}\right)} - - - - - - - - - - - - (\mathrm{S11})$$

$$I = I_0 + A_1 \times e^{(-x/t_f)} - - - - - - - - - - - (\mathrm{S12})$$

I = current

I_0 = initial value of current

A_1 = independent variables

t_r = rise time, t_f = fall time, x = time

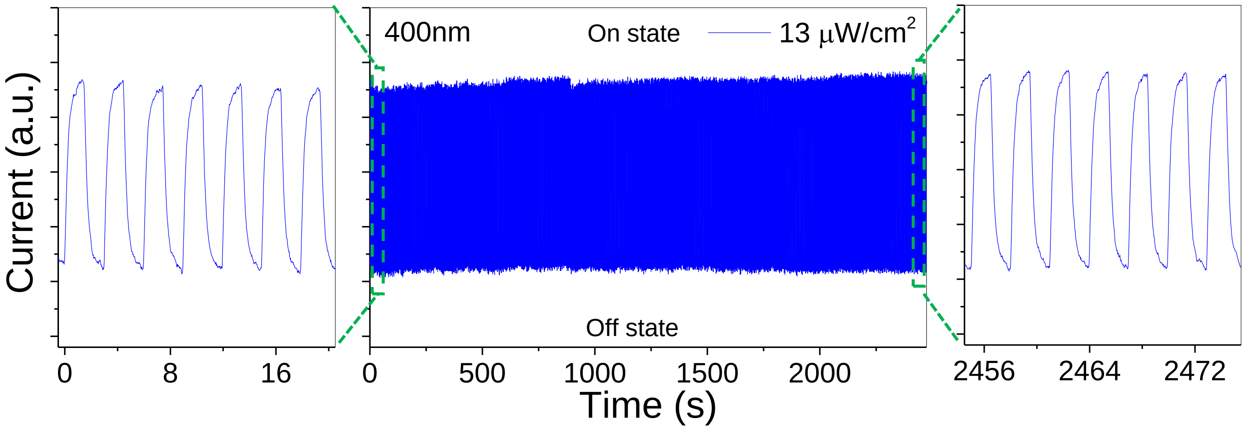

Figure S21. Transient photocurrent stability of Cs$_3$Bi$_2$Br$_3$I$_{5.2}$ based photodetector with 828 on-off cycles under 0.3 Hz 450nm light illumination.

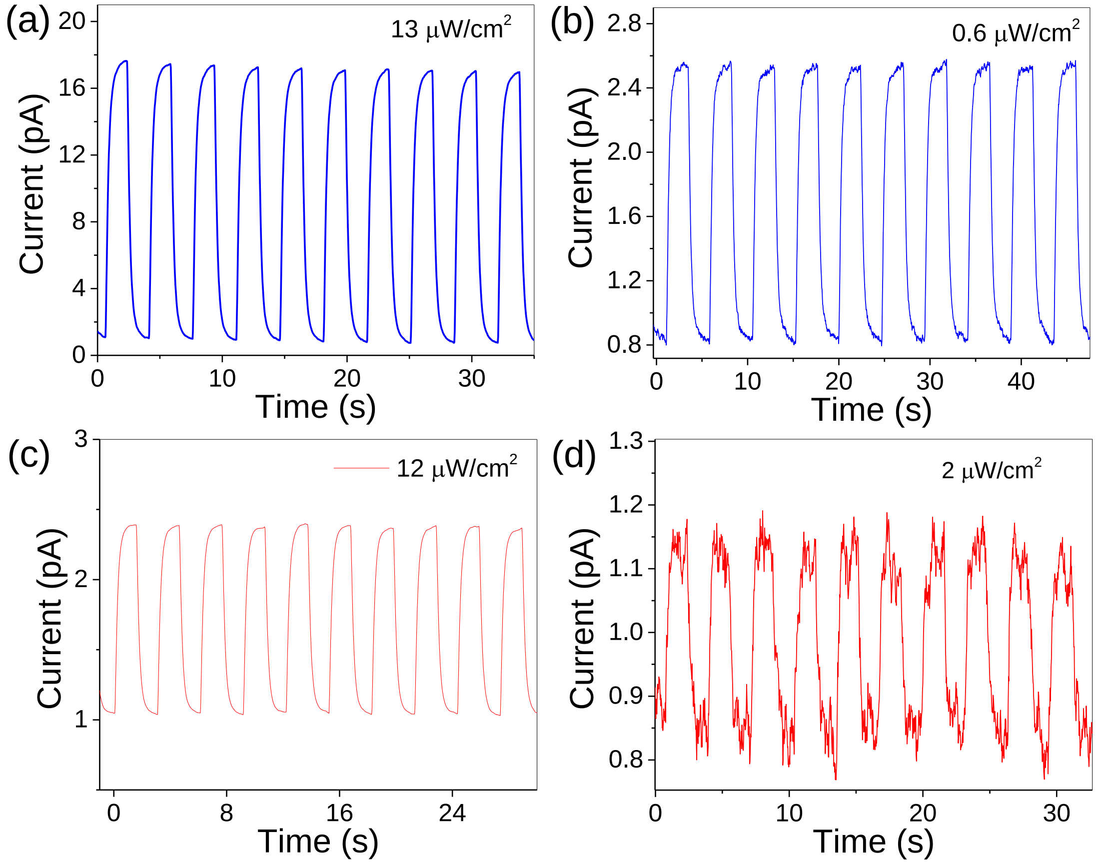

Figure S22. Real-time photocurrent response of the photodetector under 450 nm light at intensities of (a) 13 µW/cm² and (b) 0.6 µW/cm², and under 650 nm light at intensities of (c) 12 µW/cm² and (d) 0.7 µW/cm².

Table S11: Comparison of Bi-based halide perovskite self-powered photodetector performance in the literature

Sl. No.	**Material (structure)**	**Morphology**	**Device structure**	**R (A/W)**	**D (Jones)**	**Range of detection**	**Reference**
1.	$Cs_3Bi_2Br_3I_{5.2}$ (2D)	MC	Au/$Cs_3Bi_2Br_3I_{5.2}$/ ITO	0.9	1.6×10^{12} @ 540 nm	Visible and NIR	Our work
2.	$Cs_3Bi_2I_9$ (0D)	TF	FTO/$Cs_3Bi_2I_9$/ Ag	7.29×10^{-8}	2.17×10^{3}	Visible	[19]
3.	$Cs_3Bi_2I_9$ (0D)	MC	ITO/SnO_2/ $Cs_3Bi_2I_9$/ PTAA/Au/ITO	0.052	2.9×10^{11} @ 405 nm	Visible	[20]
4.	$Cs_3Bi_2I_6Br_3$ (2D)	TF	ITO/PEDOT:PSS/ $Cs_3Bi_2I_6Br_3$/C_{60}/BCP/Ag	0.015	4.6×10^{11} @ 400 nm	Visible	[21]
5.	$Cs_3Sb_2I_9$ (2D)	TF	Au/PolyTPD/ $Cs_3Sb_2I_{9-x}Cl_x$/TiO_2/FTO	0.062	3.5×10^{12} @ 505 nm	Visible	[22]

6.	$Cs_3Sb_2I_{9-x}Cl_x$ (2D)	TF	$Au/PolyTPD/Cs_3Sb_2I_{9-x}Cl_x/TiO_2/FTO$	0.205	6.1×10^{12} @ 505 nm	Visible	22
7.	$Rb_3Sb_2I_9$ (0D)	TF	$Au/PolyTPD/Rb_3Sb_2I_9/TiO_2/FTO$	0.174	4.3×10^{12} @ 505 nm	Visible	22
8.	$Cs_2AgBiBr_6$ (3D)	TF	$Au/Cs_2AgBiBr_6/SnO_2/ITO$	0.0001	2.1×10^{10} @ 350 nm	Visible	23
9.	$Cs_3Bi_2Br_9$ (2D)	TF	$ITO/NiO_x/Cs_3Bi_2Br_9/Au$	0.0043	1.3×10^{11} @ 420 nm	Visible	24
10.	Ns-$MA_3Bi_2I_9$ (0D)	TF	FTO/c-TiO_2/ Ns-$MA_3Bi_2I_9$ /graphite	0.0001	0.61×10^{7} @ 480 nm	Visible	25

Table S12. Rise and Decay Times for $Cs_3Bi_2Br_3I_{5.2}$-Based Photodetector Under Band-to-Band and Mid-Gap Light Illumination

S. No.	**Absorption Region**	**Wavelength (nm)**	**Rise time (T_r, ms)**	**Decay time (T_d, ms)**
1	Band to band	450	238	248
2	Mid-gap	650	144	163

Note and references

1 P. R. Jubu, F. K. Yam, V. M. Igba and K. P. Beh, *J. Solid State Chem.*, 2020, **290**, 121576.

2 G. Kresse and J. Hafner, *Phys. Rev. B*, 1994, **49**, 14251–14269.

3 G. Kresse and J. Hafner, *Phys. Rev. B*, 1993, **47**, 558–561.

4 D. Joubert, *Phys. Rev. B - Condens. Matter Mater. Phys.*, 1999, **59**, 1758–1775.

5 G. Kresse and J. Furthmüller, *Phys. Rev. B*, 1996, **54**, 11169–11186.

6 J. P. Perdew, K. Burke and M. Ernzerhof, *Phys. Rev. Lett.*, 1996, **77**, 3865–3868.

7 J. D. Pack and H. J. Monkhorst, *Phys. Rev. B*, 1977, **16**, 1748–1749.

8 K. Momma and F. Izumi, *J. Appl. Crystallogr.*, 2011, **44**, 1272–1276.

9 A. M Ganose, A. J Jackson and D. O Scanlon, *J. Open Source Softw.*, 2018, **3**, 717.

10 M. Leng, Y. Yang, K. Zeng, Z. Chen, Z. Tan, S. Li, J. Li, B. Xu, D. Li, M. P. Hautzinger, Y. Fu, T. Zhai, L. Xu, G. Niu, S. Jin and J. Tang, *Adv. Funct. Mater.*, 2018, **28**, 1704446 (1–11).

11 J. Gu, G. Yan, Y. Lian, Q. Mu, H. Jin, Z. Zhang, Z. Deng and Y. Peng, *RSC Adv.*, 2018,

8, 25802–25807.

12 M. Y. Valakh, M. P. Lisitsa, E. Y. Peresh, O. V. Trylis and A. M. Yaremko, *J. Mol. Struct.*, 1997, **436–437**, 309–313.

13 P. Acharyya, K. Pal, A. Ahad, D. Sarkar, K. S. Rana, M. Dutta, A. Soni, U. V. Waghmare and K. Biswas, *Adv. Funct. Mater.*, 2023, **33**, 1–10.

14 M. Bouzidi, M. Ben Bechir, D. R. Almalawi, I. H. Smaili, F. Aljuaid and N. I. Aljuraide, *Opt. Mater. (Amst).*, 2024, **154**, 115640.

15 V. M. Le Corre, E. A. Duijnstee, O. El Tambouli, J. M. Ball, H. J. Snaith, J. Lim and L. J. A. Koster, *ACS Energy Lett.*, 2021, **6**, 1087–1094.

16 Y. Liu, Z. Xu, Z. Yang, Y. Zhang, J. Cui, Y. He, H. Ye, K. Zhao, H. Sun, R. Lu, M. Liu, M. G. Kanatzidis and S. (Frank) Liu, *Matter*, 2020, **3**, 180–196.

17 D. Shi, V. Adinolfi, R. Comin, M. Yuan, E. Alarousu, A. Buin, Y. Chen, S. Hoogland, A. Rothenberger, K. Katsiev, Y. Losovyj, X. Zhang, P. A. Dowben, O. F. Mohammed, E. H. Sargent and O. M. Bakr, *Science (80-.).*, 2015, **347**, 519–522.

18 K. D. M. Rao, M. Hossain, Umesh, A. Roy, A. Ghosh, G. S. Kumar, P. Moitra, T. Kamilya, S. Acharya and S. Bhattacharya, *Nanoscale*, 2020, **12**, 11986–11996.

19 S. Devasia, S. Shaji, D. A. Avellaneda, J. A. A. Martinez and B. Krishnan, *J. Alloys Compd.*, 2022, **893**, 162294.

20 K. Dong, H. Zhou, M. Xiao, P. Gui, Z. Gao, F. Yao, W. Shao, C. Liu, C. Tao, W. Ke and G. Fang, *Appl. Phys. Lett.*, 2022, **120**, 1312–1317.

21 D. Liu, B.-B. Yu, M. Liao, Z. Jin, L. Zhou, X. Zhang, F. Wang, H. He, T. Gatti and Z. He, *ACS Appl. Mater. Interfaces*, 2020, **12**, 30530–30537.

22 J. Mei, M. Liu, P. Vivo and V. Pecunia, *Adv. Funct. Mater.*, 2021, **31**, 2106295.

23 L. Z. Lei, Z. F. Shi, Y. Li, Z. Z. Ma, F. Zhang, T. T. Xu, Y. T. Tian, D. Wu, X. J. Li and G. T. Du, *J. Mater. Chem. C*, 2018, **6**, 7982–7988.

24 Y. Liu, Y. Gao, J. Zhi, R. Huang, W. Li, X. Huang, G. Yan, Z. Ji and W. Mai, *Nano Res.*, 2022, **15**, 1094–1101.

25 A. Bhorde, S. Nair, H. Borate, S. Pandharkar, R. Aher, A. Punde, A. Waghmare, P. Shinde, P. Vairale, R. Waykar, V. Doiphode, V. Jadkar, Y. Hase, S. Rondiya, N. Patil, M. Prasad and S. Jadkar, *New J. Chem.*, 2020, **44**, 11282–11290.